



# Strongly enhanced sensitivities of CMOS compatible plasmonic titanium nitride nanohole arrays for refractive index sensing under oblique incidence

WEIJIA HAN,<sup>1,2,\*</sup>  SEBASTIAN REITER,<sup>2</sup> JON SCHLIPF,<sup>2</sup>   
CHRISTIAN MAI,<sup>3</sup> DAVIDE SPIRITO,<sup>3</sup>  JOSMY JOSE,<sup>3</sup> CHRISTIAN  
WENGER,<sup>3,4</sup> AND INGA A. FISCHER<sup>2,5</sup>

<sup>1</sup>School of Mathematical and Physical Sciences, Wuhan Textile University, Wuhan 430200, China

<sup>2</sup>Experimental Physics and Functional Materials, Brandenburgische Technische Universität Cottbus-Senftenberg, Erich-Weinert-Straße 1, 03046 Cottbus, Germany

<sup>3</sup>IHP—Leibniz-Institut für innovative Mikroelektronik, Im Technologiepark 25, 15236 Frankfurt (Oder), Germany

<sup>4</sup>Semiconductor Materials, Brandenburg University of Technology Cottbus-Senftenberg (BTU), 03046 Cottbus, Germany

<sup>5</sup>inga.fischer@b-tu.de

\*weijia.han@b-tu.de

**Abstract:** Titanium nitride (TiN) is a complementary metal-oxide-semiconductor (CMOS) compatible material with large potential for the fabrication of plasmonic structures suited for device integration. However, the comparatively large optical losses can be detrimental for application. This work reports a CMOS compatible TiN nanohole array (NHA) on top of a multilayer stack for potential use in integrated refractive index sensing with high sensitivities at wavelengths between 800 and 1500 nm. The stack, consisting of the TiN NHA on a silicon dioxide (SiO<sub>2</sub>) layer with Si as substrate (TiN NHA/SiO<sub>2</sub>/Si), is prepared using an industrial CMOS compatible process. The TiN NHA/SiO<sub>2</sub>/Si shows Fano resonances in reflectance spectra under oblique excitation, which are well reproduced by simulation using both finite difference time domain (FDTD) and rigorous coupled-wave analysis (RCWA) methods. The sensitivities derived from spectroscopic characterizations increase with the increasing incident angle and match well with the simulated sensitivities. Our systematic simulation-based investigation of the sensitivity of the TiN NHA/SiO<sub>2</sub>/Si stack under varied conditions reveals that very large sensitivities up to 2305 nm per refractive index unit (nm RIU<sup>-1</sup>) are predicted when the refractive index of superstrate is similar to that of the SiO<sub>2</sub> layer. We analyze in detail how the interplay between plasmonic and photonic resonances such as surface plasmon polaritons (SPPs), localized surface plasmon resonances (LSPRs), Rayleigh Anomalies (RAs), and photonic microcavity modes (Fabry-Pérot resonances) contributes to this result. This work not only reveals the tunability of TiN nanostructures for plasmonic applications but also paves the way to explore efficient devices for sensing in broad conditions.

Published by Optica Publishing Group under the terms of the [Creative Commons Attribution 4.0 License](https://creativecommons.org/licenses/by/4.0/). Further distribution of this work must maintain attribution to the author(s) and the published article's title, journal citation, and DOI.

## 1. Introduction

Technological evolution drives an ever increasing demand for low-cost sensing devices. To that end, plasmonic sensors that allow label free, rapid detection of biochemical substances in real time have been widely investigated and applied in biological sensing and imaging, chemical industry, food safety monitoring and environmental sensing among other application areas [1,2].

Plasmonic sensing is based either on the excitation of collective electron oscillations (surface plasmons) along the interface of metal/dielectric that resonantly interact with incident light, which typically occurs in the form of propagating surface plasmon polaritons (SPPs), or non-propagating localized surface plasmon resonances (LSPRs) [3,4]. The wavelengths of resonances are highly sensitive to the change in refractive index of the surrounding dielectric [5]. This effect can be used for refractive index (RI) sensing, i.e. monitoring RI changes adjacent to the metal/dielectric interface by quantifying the ratio of resonance wavelength shift  $\Delta\lambda_R$  to RI shift  $\Delta n$ . When the metal surface is functionalized with molecules that selectively bind to analytes, these binding events lead to a modification of the RI close to the sensor surface – this effect is utilized for label-free biosensing of the analytes. The detection of bulk refractive index changes has relevance e.g. for monitoring the properties of liquids.

In this context, surface plasmon mediated extraordinary optical transmission (EOT) through arrays of subwavelength holes in a metal film, as first reported by Ebbesen in 1998 [6], has been explored for detecting RI changes [7,8]. The optical properties of such nanohole arrays (NHAs) result from the complex interplay of interference, diffraction and plasmonic resonances. Transmission peaks in NHAs in particular have been argued to involve SPPs at the interface between the metal film and the adjacent dielectric as well as so-called Rayleigh anomalies (RAs) originating from the diffraction of light parallel to the NHA surface [9,10]. The interference between these excitations and a spectrally broad continuum e.g. provided by direct hole transmission results in narrow [9,11], asymmetric peak shapes in the form of Fano resonances [12].

So far, most of the investigated plasmonic nanostructures are fabricated from noble metals. While those exhibit excellent optical properties [13–16], they can be unstable at high temperatures or in corrosive environments, have low mechanical durability and, most importantly, are incompatible with complementary metal-oxide-semiconductor (CMOS) fabrication processes [17]. Using CMOS compatible metals instead not only makes advanced industrial methods available for large-scale high precision fabrication of nanostructures, it also opens up a path towards on-chip integration of plasmonic structures with optoelectronic devices for integrated sensors that no longer rely on expensive and bulky instrumentation for read-out [18–20].

A large number of alternative CMOS-compatible materials have been explored for use in plasmonic applications, such as aluminum [19], tungsten [21], and metal nitrides [22]. Here, TiN is a promising candidate for plasmonic applications because of its high chemical and thermal robustness and biocompatibility. TiN nanostructures have been investigated for broadband absorption [23], efficient local heating transducers [24], and hyperbolic metamaterials [25,26]. Recently, the integration of plasmonic TiN-based nano-hole-arrays on Ge photodetectors in a 200 mm wafer CMOS compatible silicon technology has been successfully shown, which paves the way for the large-scale fabrication of refractive index sensors based on such structures [27]. However, ohmic losses are considerably higher in TiN compared to e.g. Au. These impact resonance widths and lead to fast plasmon decay, which can be potentially limiting for applications, especially for refractive index sensing [24].

In this work, after having shown that TiN nanohole arrays can be fabricated using industrial fabrication processes [27], we investigated TiN nanohole arrays with square configurations of nanoholes on an SiO<sub>2</sub>/Si layer stack both theoretically and experimentally specifically for potential use in integrated RI sensing. This is motivated by our aim to utilize TiN nanohole arrays in conjunction with Ge photodetectors for integrated refractive index sensors. Depositing the TiN NHA onto a multi-layered substrate is, on the one hand, necessary for any kind of device integration, on the other hand it provides additional parameters for improving sensor performance. Morphological details and optical properties were investigated by atomic force microscopy (AFM), scanning electron microscopy (SEM) and spectroscopic ellipsometry. Reflectance spectra obtained by spectroscopic characterization were reproduced with high accuracy by

numerical simulation *via* both finite difference time domain (FDTD) and rigorous coupled-wave analysis (RCWA) methods. Extracted sensitivities from experimental reflectance spectra increase with increasing incident angle while these values are matched well with the simulated results.

Using our experimental data for the calibration of simulation, we systematically investigated how sensor performance can be tuned by adjusting the angle of light incidence as well as the geometry of the layer stack below the TiN NHA. We observe an increase in sensitivity by almost a factor of two when increasing the angle of incidence from 20° to 70° in experiment. Compared to previous investigations, which report an increase in sensitivity with increasing angle of incidence [28], this magnitude of the effect is striking. Furthermore, using simulations, we predict sensitivities well above 2000nm RIU<sup>-1</sup> in our structures under certain conditions and explore how the coupling between plasmonic and photonic resonant modes contribute to this result. Our investigation shows that a careful tuning of few parameters can boost sensor performance to the point where TiN NHAs can become competitive for use in integrated, CMOS compatible plasmonic sensors.

## 2. Devices and methods

### 2.1. Device fabrication and optical characterizations

The TiN NHA/SiO<sub>2</sub>/Si stack was obtained by a well-developed industrial fabrication process conducted in IHP GmbH - Leibniz Institute for High Performance Microelectronics [27]. A layer of SiO<sub>2</sub> was deposited on a clean p-type 8" Si wafer by plasma enhanced chemical vapour deposition (PECVD) with tetraethoxysilane (TEOS) as the carrier gas. A TiN film with a thickness of 100 nm was deposited onto the SiO<sub>2</sub> surface by a reactive magnetron sputtering process using titanium as target material with pure Ar/N<sub>2</sub> (Ar: 98 sccm, N<sub>2</sub>: 2 sccm) as carrier gases. A mask with square arrays of nanoholes with sizes of 3 × 3 mm<sup>2</sup> including parameters of periodicity/diameter: 700 nm/540 nm (P700D540) and 500 nm/360 nm (P500D360) was used to pattern the photoresist coated TiN film, afterwards a reactive ion etching (RIE) system was used to etch the exposed area to perforate the TiN film for the generation of nanoholes. Removal of photoresist was carried out by dipping into acetone solvent after etching. The TiN NHA/SiO<sub>2</sub>/Si samples were rinsed with deionized water and dried with compressed nitrogen flow for further use.

A morphological AFM image of the sputtered TiN films was obtained in tapping mode, and the corresponding surface roughness was analyzed by the built-in algorithm. The structured samples were characterized in a SEM Zeiss MERLIN Gemini 2 by using a secondary electron detector of In-Lens mode with the primary beam set to a voltage of 1.50 kV. The average diameter of the nanoholes was evaluated by the ImageJ software. To check the detailed edge of the nanoholes, a cross-sectional SEM image in secondary electron mode with an incident angle of 54° was also obtained, where a decoration layer consisting of 15 nm oxide and 50 nm nitride was deposited to enhance image contrast (Figure S4 (b)).

To obtain the dielectric permittivity of TiN film, ellipsometry measurements were conducted with a variable angle spectroscopic ellipsometer (Sentech SE 850) from the ultraviolet to near-infrared wavelength range (200 to 2200 nm). Reflectance spectroscopic measurements on TiN NHA/SiO<sub>2</sub>/Si devices were carried out in a LAMBDA 1050 UV/Vis/NIR Spectrophotometer (PerkinElmer, Inc.) with a Total Absolute Measurement System (TAMS), a snap-in integrating sphere and a Si/InGaAs detector. In this setup, spectra under varied excitation angles were obtained using a spot size with a diameter of approx. 2 mm. Under illumination with a *p*-polarized light source with varied incident angle (10°, 20°, 30°, 40°, 50°, 60° and 70°), the reflectance spectra of sample P700D540 and P500D360 in air were obtained in a spectral range of 800–1600 nm with an interval of 5 nm. We note that transmittance spectra for the samples could not be reliably obtained as a result of free carrier absorption in the Si wafer as well as an unpolished backside, which led to strong signal suppression.

For the measurements in water and acetone under  $p$ -polarized excitation with varied incident angle, a regular cylindrical beaker was employed to hold the liquid in the middle of the sample stage. The sample was fixed in the middle the beaker to keep the incidence light and reflected light perpendicular to the beaker's surface to avoid refraction dissipation, as shown in Fig. S1. The baseline was measured in transmission.

## 2.2. Optical simulation methods

Two different methods (using the commercial finite-difference time-domain (FDTD) solutions software package by Ansys Lumerical and the rigorous coupled-wave analysis (RCWA) method) were employed for simulations [29,30]. The use of the two simulation methods allows us to make use of their specific advantages (such as lower simulation times for RCWA and the possibility to extract electric field distributions for the full wavelength range for FDTD simulations) while also having independent verification of our main simulation results. The dielectric constant of the TiN layer was obtained from the spectroscopic ellipsometry (SE) (Figs. 1(b) and 1(c)), the permittivity data of SiO<sub>2</sub> and Si were taken from literature [31,32].

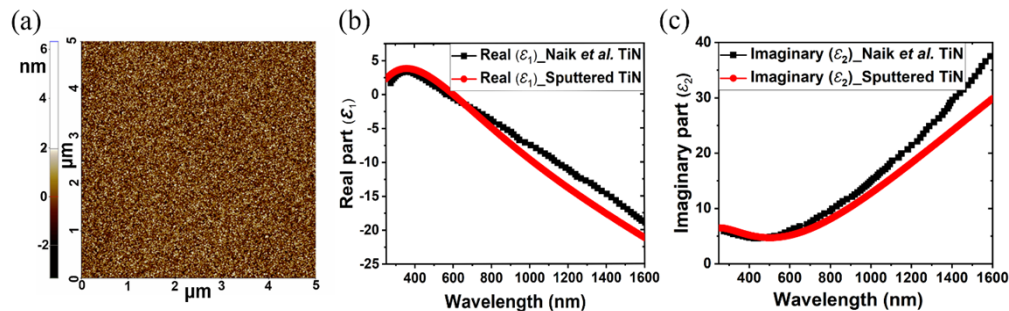


**Fig. 1.** AFM topographical image (a) of the sputtered TiN film, real (b) and imaginary (c) parts of the permittivity of sputtered TiN film obtained by spectroscopic ellipsometry compared with Ref. [33].

For FDTD simulations, a plane wave light source with a wide wavelength range in UV-vis-NIR was set in the surrounding superstrate above the TiN NHA (Fig. 2(a)). A frequency-domain field and power monitor situated at the interface of TiN NHA/SiO<sub>2</sub> was set to collect the transmission and another frequency-domain field and power monitor was placed in the plane at  $z = 300$  nm for reflectance spectra. Periodic boundary conditions, and perfectly matched layers were applied in  $y$ , and  $z$  direction, respectively. The mesh size along  $x$ ,  $y$  and  $z$  direction is  $3 \text{ nm} \times 3 \text{ nm} \times 3 \text{ nm}$ . For oblique incidence, the light source was set to a plane wave type of broadband fixed angle source technique (BFAST) mode to keep incidence constant with varied excitation angles. Electric field distributions were obtained by setting a frequency domain power monitor to collect electric fields on top surface of TiN NHA, at the interface of TiN NHA and SiO<sub>2</sub>, and of the cross-section profiles of TiN NHA/SiO<sub>2</sub>/Si.

For RCWA calculation, the unit cell was set as the parameters obtained from the fabricated devices with a transverse magnetic (TM) or transverse electric polarized plane wave as light source. A 10th diffraction order and periodic boundary conditions in enhanced transmission matrix method were used to calculate the reflectance and transmittance spectra.

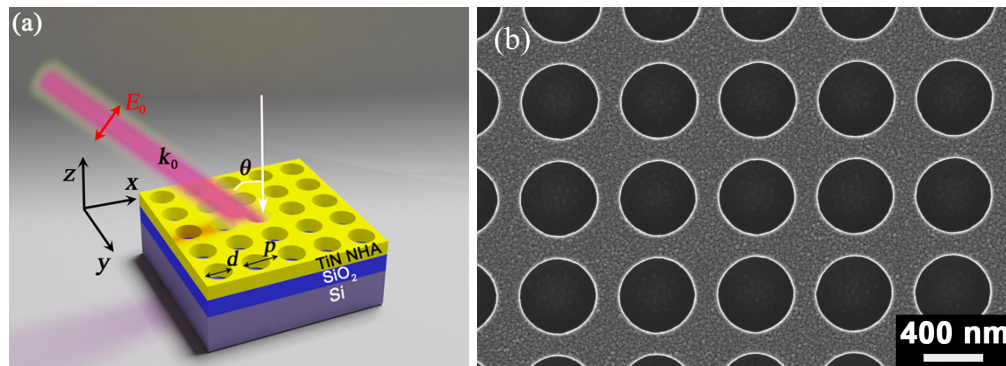


**Fig. 2.** Schematic diagram (a) and morphological SEM image of the fabricated TiN NHA/SiO<sub>2</sub>/Si device P700D540.

### 3. Results

#### 3.1. Material and structural characterization

A root mean square (RMS) roughness of  $\sim 1.0$  nm obtained from AFM measurements (Fig. 1(a)) indicates that a relatively smooth TiN film was successfully prepared.

The real and imaginary part of the relative permittivity  $\varepsilon_r = \varepsilon_1 + i\varepsilon_2$  of the unstructured TiN film (Figs. 1(b) and 1(c)) was obtained from spectroscopic ellipsometry measurements based on fitting with a harmonic oscillator model and compared with previously reported data. The  $\varepsilon_1$  spectrum (red square in Fig. 1(b)) shows a crossover wavelength  $\lambda_0$  of 581 nm. As discussed e.g. by Patsalas et al. [34], both the real and the imaginary part of the permittivity of TiN films can show large variations depending on the deposition method as well as the deposition parameters. Comparing with the  $\varepsilon_1$  spectrum of TiN film obtained from DC reactive sputtering reported by Naik *et al.* in Fig. 1(b) [33], our measured  $\varepsilon_1$  curve (red square) overlaps with the real part of Naik *et al.* TiN (black square) from 200 nm to 700 nm while being slightly lower in the range of 700–1600 nm. The imaginary part of the permittivity is related to the degree of optical loss in the film. The magnitude of the  $\varepsilon_2$  spectrum (red squares in Fig. 1(c)) shows a minimum value around the screened plasmon wavelength (581 nm) and is lower than the imaginary part of TiN (black square in Fig. 1(c)) prepared by Naik *et al.* from 500 nm to 1600 nm [33], which indicates slightly lower losses in our sputtered TiN film. Furthermore, plasmonic properties of our TiN film were assessed by determining a quality factor for LSPRs ( $-\varepsilon_1/\varepsilon_2$ ) based on assumption of spherical nanoparticles under the quasi-static regime (Fig. S3(a)) and a quality factor for SPPs ( $\varepsilon_1^2/\varepsilon_2$ ) (Fig. S3(b)) in the Supplement 1 [17].

The structured sample containing a NHA in the TiN film is shown schematically in Fig. 2(a). The SEM image in Fig. 2(b) indicates that highly ordered square arrays of nanoholes were obtained. The lattice pitch ( $p$ ) and hole diameter ( $d$ ) on average are 700 nm and 540 nm and referred to as sample P700D540, respectively, as determined by software Image J [35]. This is in perfect agreement with the geometrical parameters of the mask. Moreover, the structuring process has been found to leave the surface roughness of the TiN NHA unaffected.

#### 3.2. Optical characterization and simulation of reflectance spectra

Reflectance spectra of TiN NHA/SiO<sub>2</sub>/Si stack P700D540 under illumination with a  $p$ -polarized light source at incident angles ( $\theta$ ) of 10°, 20°, 30° and 40° to the vertical axis, respectively, are shown in Fig. 3(a). A resonant dip in the reflectance spectrum (black curve) can be seen at around 985 nm under an excitation angle of 10°. When tuning the incident angle to 20°, 30° and 40°, the corresponding dip wavelength red-shifts to 1025 nm, 1105 nm and 1192 nm, respectively. At

incident angles above  $20^\circ$ , the resonances exhibit asymmetric Fano profiles corresponding to a sharp local maximum followed by an adjacent minimum [12].

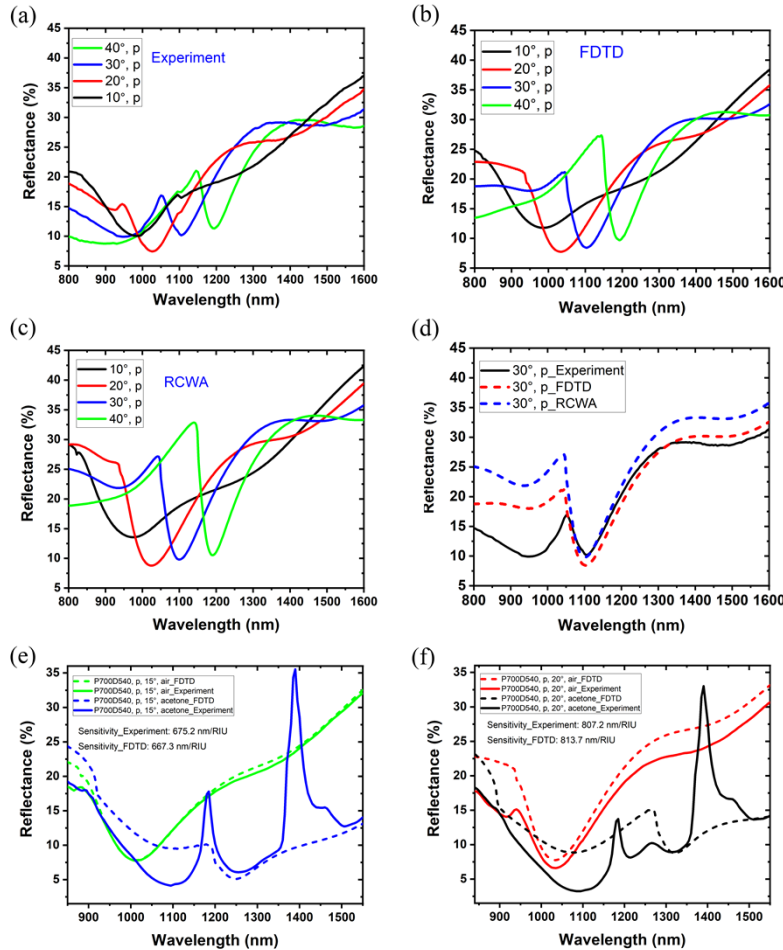


**Fig. 3.** Reflectance spectra of TiN NHA/SiO<sub>2</sub>/Si stack P700D540 under *p*-polarized excitation with varied angles of  $10^\circ$ ,  $20^\circ$ ,  $30^\circ$  and  $40^\circ$  in air by experimentally spectroscopic characterization (a), by FDTD simulation (b) and by RCWA method (c). Comparison of measured reflectance and simulated spectra via FDTD and RCWA of TiN NHA/SiO<sub>2</sub>/Si P700D540 under *p*-polarized excitation with an angle of  $30^\circ$  (d). Reflectance spectra of P700D540 under *p*-polarized excitation at angles of  $15^\circ$  (e) and  $20^\circ$  (f) in acetone and in air, compared with the corresponding simulated spectra.

The spectra obtained using FDTD (Fig. 3(b)) and RCWA simulations (Fig. 3(c)) exhibit the same trends as those demonstrated in experiment (Fig. 3(a)). The resonance wavelengths show obvious redshifts at increasing angle of incidence and are positioned at 985 nm, 1029 nm, 1103 nm and 1192 nm in the spectra obtained by FDTD simulations, compared with 982 nm, 1025 nm, 1099 nm and 1190 nm by RCWA method, respectively. For comparison, Fig. 3(d) displays the reflectance spectra of TiN NHA/SiO<sub>2</sub>/Si under an incident angle of  $30^\circ$  by spectroscopic characterization (black curve), by FDTD (red dashed line) and by RCWA (blue dashed line). We find excellent agreement between the simulated and measured spectra in terms of the resonance dip wavelengths. Remaining discrepancies from 1050 nm to 1300 nm in simulated and measured reflectance spectra can be attributed to the subtle imperfections of the fabricated TiN NHAs, such

as surface and edge roughnesses. Given the fact that optical data is collected over several square mm of the fabricated structures as the photo of the fabricated chip in Fig. S2 shows, our results nonetheless attest to their excellent homogeneity.

Since the wavelength of the plasmonic resonance is extremely sensitive to the dielectric properties of metal layer and the interfaced medium, changes of the RI  $\Delta n$  of the surrounding medium result in a wavelength shift  $\Delta\lambda_R$ . A commonly used quantity to evaluate sensor performance in this context is the sensitivity  $S$  defined as  $S = \Delta\lambda_R/\Delta n$ . Fig. S5(a) displays the reflectance spectra of TiN NHA/SiO<sub>2</sub>/Si stack P700D540 under  $p$ -polarized excitation with varied angles of 10°, 15°, 20°, 30° and 40° in acetone ( $n = 1.3586$ ). Because of the strong absorption of acetone at wavelength ranges of 1150-1200 nm and 1370-1500 nm [36], resonance dips in those wavelength ranges cannot be observed in experiment. Nonetheless, the resonance wavelengths at 1252 nm (Fig. 3(e) blue solid curve) and 1321 nm (Fig. 3(b) red solid curve) of TiN NHA/SiO<sub>2</sub>/Si stack P700D540 at incidence angle of 15° and 20° can be used to determine the sensitivities when comparing with the corresponding reflectance spectra obtained in air. The sensitivity (675.2 nm/RIU) extracted from the measured reflectance spectra in air and in acetone at incidence angle of 15° is slightly higher than the calculated sensitivity (667.3 nm/RIU, Fig. 3(e)), while the measured sensitivity (807.2 nm/RIU) at 20° is slightly lower the simulated value (813.7 nm/RIU) in Fig. 3(f). A clear increase in sensitivity is realized by increasing the angle of incidence.

To facilitate the measurement of sensitivities at higher incidence angles, a TiN NHA/SiO<sub>2</sub>/Si stack with a lower lattice pitch (500 nm) and hole diameter (360 nm) was also investigated (see Fig. S7 for an SEM image). This sample is referred to as P500D360. The reflectance spectra of P500D360 in air are obtained by spectroscopy characterization (Fig. 4(a)). Again, the resonance dips can be seen to red-shift with increasing incident angle, however, the agreement between experimental results and simulated spectra (Fig. S8) is not as good as for sample P700D540. We attribute this to the larger fabrication challenges associated with the smaller structure sizes, which can lead to larger inhomogeneities on the scales probed in measurement. Our spectra show that the resonance width decreases with the increasing incident angle, as evidenced by the reduction in full width at half maximum (FWHM) of the resonance dip extracted from the simulated spectra (see inserted image of Fig. 4(b)). This is particularly important for our samples, for which resonances in the reflectance spectra exhibit large linewidths at small angles of incidence as a result of large ohmic losses in the TiN. The increase of incident angle can, on the one hand, enhance the interaction of different resonant modes, but can also boost the collection of scattered optical energy from one hole by the neighboring holes to decrease radiative losses [28,37,38]. Both effects can lead to a narrowing of the linewidth, which boosts refractive index sensing performance by facilitating the extraction of shifts in resonance wavelengths [39].

We then evaluated the bulk sensitivity of TiN NHA/SiO<sub>2</sub>/Si stack P500D360 from the reflectance spectra measured in air and in liquid. Figure 4(c) displays the measured reflectance spectra of P500D360 in acetone ( $n = 1.3586$ ) under  $p$ -polarized light source with varied incident angle. We note that features in the measured spectra at around 1180 nm and 1385 nm (marked in yellow in the Figure) are strongly influenced by absorption in acetone [36], which almost completely suppresses the signal in those wavelength ranges. The corresponding simulation results in Fig. 4(d) reveal resonance wavelengths that are in good agreement with those of the measured spectra. Most importantly, values for the sensitivity extracted from the NHA spectra in air and in liquid show a considerable increase by almost a factor of 2 as the incident angle is increased, with excellent agreement between simulation and experiment (Fig. 4(f), see also Figs. S8(a), S8(b), S8(c) and S8(f)). We note that other liquids such as water or ethanol, which are also commonly used to evaluate bulk sensitivities, all exhibit strong absorption in the wavelength range investigated here. This makes their use for experimental characterization challenging – some results on characterizing our structures in water are nonetheless shown in Fig. S8.

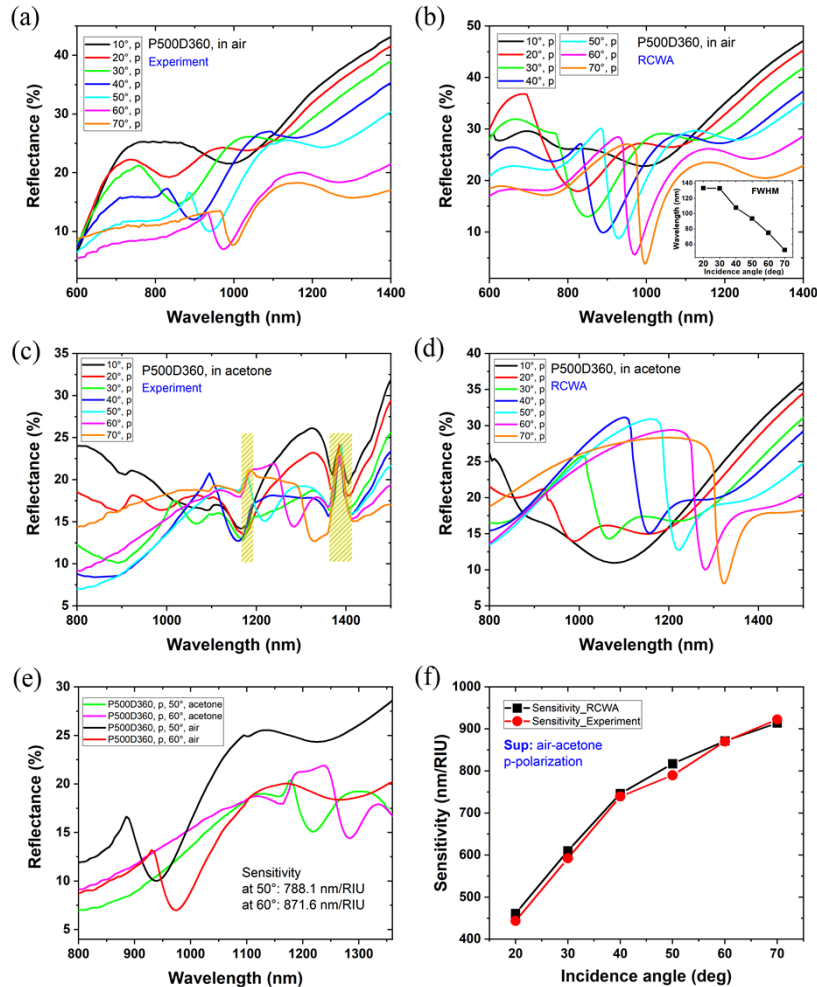


**Fig. 4.** Reflectance spectra of TiN NHA/SiO<sub>2</sub>/Si stack P500D360 under p-polarized excitation with varied angles obtained experimentally from spectroscopic characterization in air (a) and in acetone (c), and obtained by simulation (RCWA) for air (b) and for acetone (d). The full width at half maximum (FWHM) of the resonance dips in Fig. 4(b) at varied incident angles is shown by the inserted image. A comparison of measured reflectance spectra of sample P500D360 in air and in acetone at incident angle of 50° and 60° illustrates the resonance shifts (e). Sensitivities of P500D360 at incident angle of 20°, 30°, 40°, 50°, 60° and 70° are derived from both the measured and simulated reflectance spectra in air and in acetone (f).

Tuning the angle of incidence in order to boost sensitivity is a strategy that has been investigated previously [28,40]. However, our measured sensitivities increase by a factor of almost two when increasing the angle of incidence from  $20^\circ$  to  $70^\circ$  is striking compared to previous results, where e.g. switching the angle of incidence from  $30^\circ$  to  $70^\circ$  only resulted in a sensitivity increase by slightly more than 20% [28]. We, therefore, use our experimental results as a basis for a simulation-based investigation of sensor performance in various media in the following section.

#### 4. Simulation-based optimization

Anticipating the use of TiN NHAs in combination with photodetectors for integrated, CMOS-compatible sensors, we predominantly focus on the transmission characteristics in the following discussion. Furthermore, we based our investigation on sample P700D540, whose reflectance spectra show better agreement with simulation results. Since previous investigations have shown the sensitivity to be not only influenced by the angle of incidence but also by the superstrate refractive index [40,41], we focus on the influence of both parameters on sensitivities in section 4.1. We then discuss in more detail the influence of the layered substrate in the Section 4.2 based on simulation.

##### 4.1. Role of the angle of incidence and the superstrate refractive index

Transmittance spectra of TiN NHA/SiO<sub>2</sub>/Si stack P700D540 under illumination with a *p*-polarized plane wave excitation with varied incident angle from 0 to  $80^\circ$  in air as modeled in Fig. 2(a) were simulated by RCWA as shown in Fig. 5(a). An obvious Fano-like resonance can be found in each curve, where the peak position of the resonances red-shifts with increasing incident angle while the corresponding peak intensity follows a downward trend.

We, then evaluated the bulk sensitivity of TiN NHA/SiO<sub>2</sub>/Si illuminated by a *p*-polarized light source with varied incident angle using both RCWA and FDTD (Fig. 5(b)). A discussion of the optical properties under illumination with *s*-polarized light can be found in the Supplement 1 (Fig. S11). The sensitivity changes with increasing incident angle were obtained by comparing the transmittance spectra in superstrates with refractive indices of  $n = 1.0$  and  $n = 1.02$ . The results calculated by RCWA under the same simulation parameters in Fig. 5(b) (black square) show very good agreement with the FDTD results. The sensitivity exhibits a local peak at an excitation angle of  $0 \sim 15^\circ$ , whose origin will be discussed in more detail in the following, and a continuous increase at incident angles between  $\sim 15^\circ$  and  $\sim 75^\circ$  to its peak value of  $\sim 1500 \text{ nm/RIU}$ .

Because of the computational cost involved as well as the divergence of FDTD solutions when setting a high excitation angle, a systematic study of the shift of resonant wavelength for sensitivity under varied incident angle with respect to varied surrounding medium with RI changes including 1.15 to 1.16, 1.31 to 1.32, 1.44 to 1.45, and 1.61 to 1.62 was limited to RCWA calculations (Fig. 5(c)). The largest value of  $2305 \text{ nm RIU}^{-1}$  for the sensitivity is obtained under an excitation angle of  $20^\circ$  when the RI of surrounding medium is around 1.44-1.45. We note that at these values, RI matching between the superstrate (1.44-1.45) and the spacer layer ( $n_{\text{SiO}_2} = 1.45$ ) occurs. Index matching conditions have previously been shown to lead to strongly enhanced transmission through nanohole arrays [10,42].

Furthermore, to our knowledge the sensitivity of  $2305 \text{ nm RIU}^{-1}$  is the highest sensitivity predicted so far for TiN as metallization layer [43,44], and is competitive to or higher than some reported devices using noble metals (such as: gold and silver). For instance, Lesuffleur *et al.* reported a double-hole array sensor composed of two overlapping circular holes (200 nm diameter, 190 nm center spacing) in a Au film that produces two apexes in between with periodicity of 600-800 nm delivering a detection sensitivity of  $\sim 600 \text{ nm RIU}^{-1}$  from transmission measurements in air, in water, and in acetone at SP (0, 1) mode [45]. Large-area deep-silver-nanowell arrays manufactured by colloidal lithography and metal deposition reported by Yang *et al.* show a sensitivity of  $933 \text{ nm RIU}^{-1}$  [46] as the superstrate changes from water to ethanol. Chen *et al.*

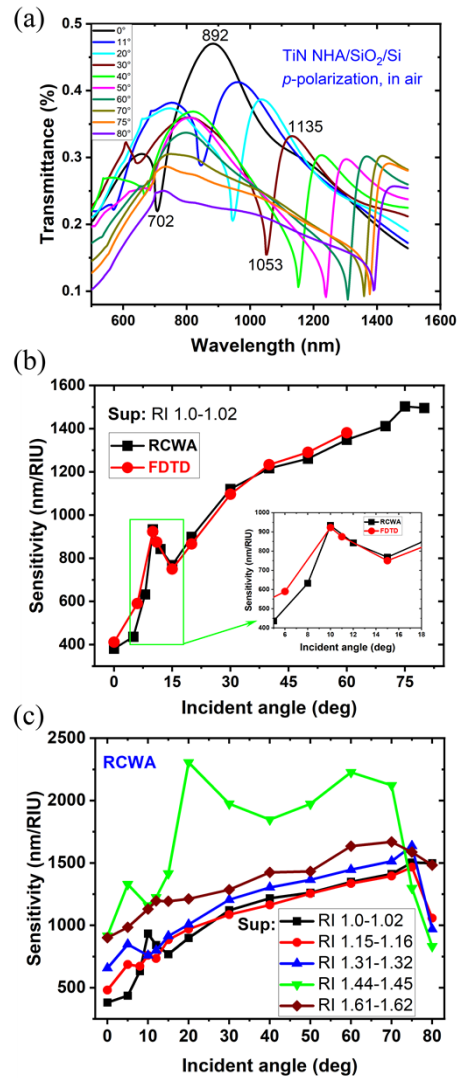


**Fig. 5.** Transmittance spectra (a) of TiN NHA/SiO<sub>2</sub>/Si device P700D540 under illumination of *p*-polarized light source with incident angle of 0°, 5°, 11°, 20°, 30°, 40°, 50°, 60°, 70°, and 80° in air. Sensitivity of TiN NHA/SiO<sub>2</sub>/Si with respect to RI change from 1.00 to 1.02 under excitation angle varied from 0° – 60° (b) by FDTD solutions (red dots) and by RCWA method (black dots), and with respect to RI changes including 1.15 to 1.16, 1.31 to 1.32, 1.44 to 1.45, and 1.61 to 1.62 under varied excitation angles by RCWA (c). The insert image in (b) shows the magnified curves for sensitivity in the angle range of 4° to 18°.

predicted a high sensitivity of 1580 nm RIU<sup>-1</sup> for a superstrate refractive index change from 1.02 to 1.05 based on a tapered nanohole arrays structure stacked by multiple cylindrical holes with the same depth but different radii [47].

The optical properties in our samples can be expected to be strongly influenced by SPPs at the interface between the TiN film and the adjacent dielectric as well as RAs resulting from the diffraction of light parallel to the NHA surface. The optical properties can also be influenced by LSPRs excited in the nanohole as well as by Fabry-Pérot resonances in the SiO<sub>2</sub> layer below the NHA that, in conjunction with the Si wafer, can act as a cavity. Here, we focus on elucidating the role those effects play in the optical properties of the investigated structures.

Analytical estimates of the SPP excitation wavelength can be obtained from the Bragg coupling condition for a 2D square array of nanoholes with periodicity  $p$  [10]

$$|\mathbf{k}_0 \sin \theta + i\mathbf{G}_x + j\mathbf{G}_y| = \text{Re} \left( \frac{\omega}{c} \sqrt{\frac{\varepsilon_m(\lambda)\varepsilon_d}{\varepsilon_m(\lambda) + \varepsilon_d}} \right), \quad (1)$$

where  $\mathbf{k}_0$ ,  $\omega$  and  $c$  are the wavevector, angular frequency and speed of incident light, respectively,  $\mathbf{G}_x$  and  $\mathbf{G}_y$  are the reciprocal lattice vectors of the 2D square NHA with  $|\mathbf{G}_x| = |\mathbf{G}_y| = \frac{2\pi}{p}$ ,  $\varepsilon_m(\lambda)$  is the wavelength dependent permittivity of the metallization layer,  $\varepsilon_d$  is the permittivity of the adjacent dielectric,  $\theta$  is the incident angle (Fig. 2(a)), and  $(i, j)$  are the integer index pairs that denote the SPP grating modes. A similar condition holds for the RAs originating from the diffracted light propagating tangentially to the surface with a more spatially extended feature than that of SPP modes. The corresponding excitation wavelengths satisfy the following equation:

$$|\mathbf{k}_0 \sin \theta + i\mathbf{G}_x + j\mathbf{G}_y| = \frac{\omega}{c} \sqrt{\varepsilon_d}. \quad (2)$$

Here, we first compare the positions of the Fano resonances in the transmittance spectra of TiN NHAs as a function of wavelength and incident angle obtained from RCWA simulations with the analytical predictions according to Eqs. (1) and (2) (Fig. 6). For a more detailed investigation of the interplay of possible resonances, transmittance diagrams are shown not only for a TiN NHA/SiO<sub>2</sub>/Si layer stack P700D540 submerged in air ( $n = 1.0$ , Fig. 6(a)), water ( $n = 1.33$ , Fig. 6(b)) and SiO<sub>2</sub> ( $n = 1.45$ , Fig. 6(c)), but also for TiN NHA/SiO<sub>2</sub> (without Si substrate, Figs. 6(d)–6(f)) and for the TiN NHA (Figs. 6(g)–6(i)). This allows us to also probe the influence of thin-film interference effects originating from the TiN/SiO<sub>2</sub> bilayer on top of the Si substrate. The scale bar represents the transmittance. We normalized all transmittance spectra with respect to the highest transmittance of TiN NHA/SiO<sub>2</sub> in air with an incident angle of 0° at wavelength of 858 nm (Fig. S12). While predictions for both SPP ( $\pm 1, 0$ ) and RA ( $\pm 1, 0$ ) resonance wavelengths according to Eqs. (1) and (2) are plotted in Fig. 6 as marked by different colors for the TiN NHA-superstrate interface, only the SPP ( $\pm 1, 0$ ) modes are shown specifically for the TiN NHA-substrate interface in Figs. 6(a), 6(b), and 6(d) and 6(e) to avoid cluttering up the Figure.

In Fig. 6(a), the SPP<sub>TiN-sup</sub>(+1, 0) (black line) and the RA<sub>sup</sub>(+1, 0) (green line) resonance wavelengths at the interface of TiN NHA and the superstrate (air) almost coincide for all incident angles. A similar behavior can be observed for the SPP<sub>TiN-sup</sub>(-1, 0) (red line) and RA<sub>sup</sub>(-1, 0) (yellow line). Furthermore, at a superstrate RI of 1.0, the analytical estimates of the resonance position show good agreement with the dips in transmittance obtained from the full wave simulation results. We also note that the incident angle  $\theta = 10^\circ$  at which a first peak in sensitivity is predicted (the insert image in Fig. 5(b)) is close to the incident angle at which the SPP<sub>TiN-sup</sub>(+1, 0) and the SPP<sub>TiN-SiO2</sub>(-1, 0) modes intersect: We attribute the enhanced sensitivity at this incident angle to an interaction of these modes. Finally, no sign of the SPP<sub>TiN-SiO2</sub>(+1, 0) mode can be found in the transmittance spectra obtained from full-wave simulation at any incident angle (Fig. 6(a)). This is in contrast to the calculated spectra for a TiN

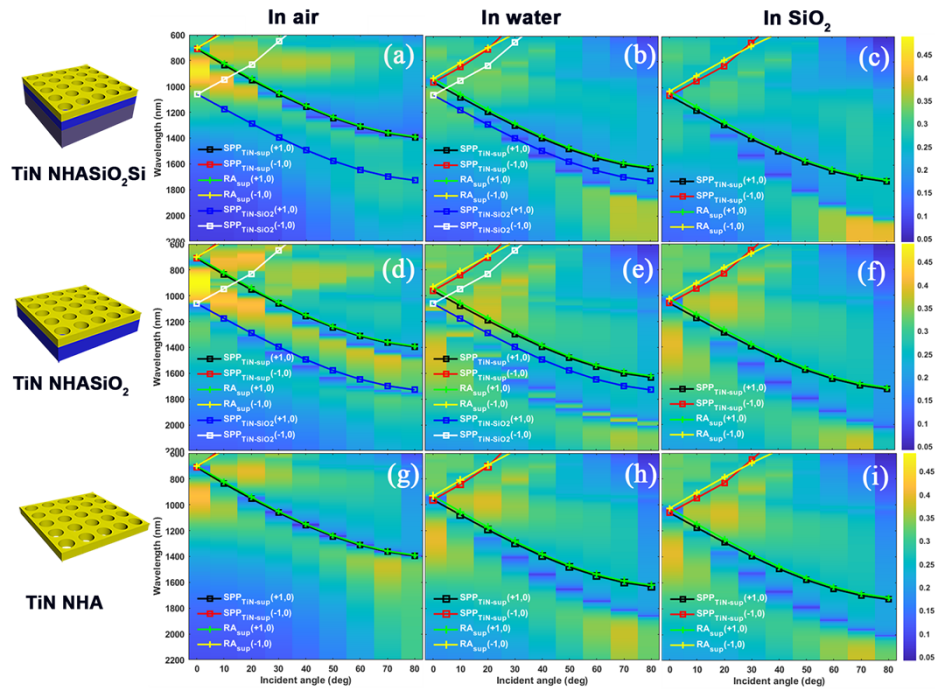


**Fig. 6.** Transmittance diagrams as a function of wavelength and incident angle of TiN NHA/SiO<sub>2</sub>/Si P700D540 (schematic at left up), TiN NHA/SiO<sub>2</sub> (schematic at left middle), and TiN NHA perforated layer (schematic at left down) under p-polarized light source with excitation angle from 0° to 80° in superstrate of air (a, d, g), of water (b, e, h), and of SiO<sub>2</sub> (c, f, i) by RCWA method, together with the calculated wavelengths of SPPs and RAs at correspondingly specific interfaces. Higher order SPP and RA modes are not shown here.

NHA/SiO<sub>2</sub> layer stack (Fig. 6(d)), where two clear dips corresponding to the SPP<sub>TiN-sup</sub>(+1, 0) and SPP<sub>TiN-SiO<sub>2</sub></sub>(+1, 0) modes appear, showing that the SPP<sub>TiN-SiO<sub>2</sub></sub>(+1, 0) mode is suppressed by the high-index Si substrate. Again, the analytical predictions are in very good agreement with the positions of the dips obtained from a full-wave simulation, this is also true for the TiN NHA entirely embedded in air (Fig. 6(g)).

For TiN NHA/SiO<sub>2</sub>/Si stack P700D540 with water (Fig. 6(b)) or SiO<sub>2</sub> (Fig. 6(c)) as superstrate, the positions of the dips obtained from full-wave simulations and under non-vertical incidence show a red shift compared to analytical estimates. This red shift becomes more pronounced with increasing angle of incidence and with increasing superstrate RI as expected from calculated sensitivities (Fig. 5(c)). Similar trends can also be observed for the TiN NHA/SiO<sub>2</sub> stack (Figs. 6(e) and 6(f)) as well as the suspended TiN NHA layer (Figs. 6(h) and 6(i)). This as well as the strong dependence of the sensitivities on the angle of incidence strongly indicates that the optical properties of our samples are influenced not only by the presence of SPPs and RAs at the NHA/superstrate interface. Indeed, in Au NHAs, increased sensitivities at oblique incidence have been attributed to the interplay of LSPRs and SPPs, whose interaction can be tuned both by the angle of incidence and the refractive index of the dielectric environment [40]. According to our simulations for the TiN NHA/SiO<sub>2</sub>/Si layer stack this leads to particularly large sensitivities when the RI of the substrate and the superstrate match (Fig. 5(c)), indicating that the coupling between LSPRs and SPPs is also particularly strong. This condition has previously been argued to lead to a coupling of the SPPs excited at the TiN-superstrate and TiN substrate interface *via* the nanoholes and, as a consequence, to strongly enhanced transmission [10].

To further investigate the interplay of resonances in our sample, we calculated electric field distributions in the near-field of TiN NHA/SiO<sub>2</sub>/Si under illumination with *p*-polarized light at an angle of 30° (Fig. 2(a)) by FDTD. We extracted the *z*-component of electric field (*E<sub>z</sub>*) at the TiN NHA/air interface, at a cross-section (*xz*-plane, *y* = 0 nm), and at the TiN NHA/SiO<sub>2</sub> interface of a TiN NHA/SiO<sub>2</sub>/Si stack both at the transmittance peak (1135 nm) and dip 1053 nm as shown in Figs. 7(a)–7(f). For comparison, the corresponding *E<sub>z</sub>* distributions under vertical incidence were also extracted at the transmittance peak 892 nm and dip 702 nm as shown in Figs. 7(g)–7(l). To clearly discern the differences among these maps, we appropriately adjusted the scale bar for all electric field images.

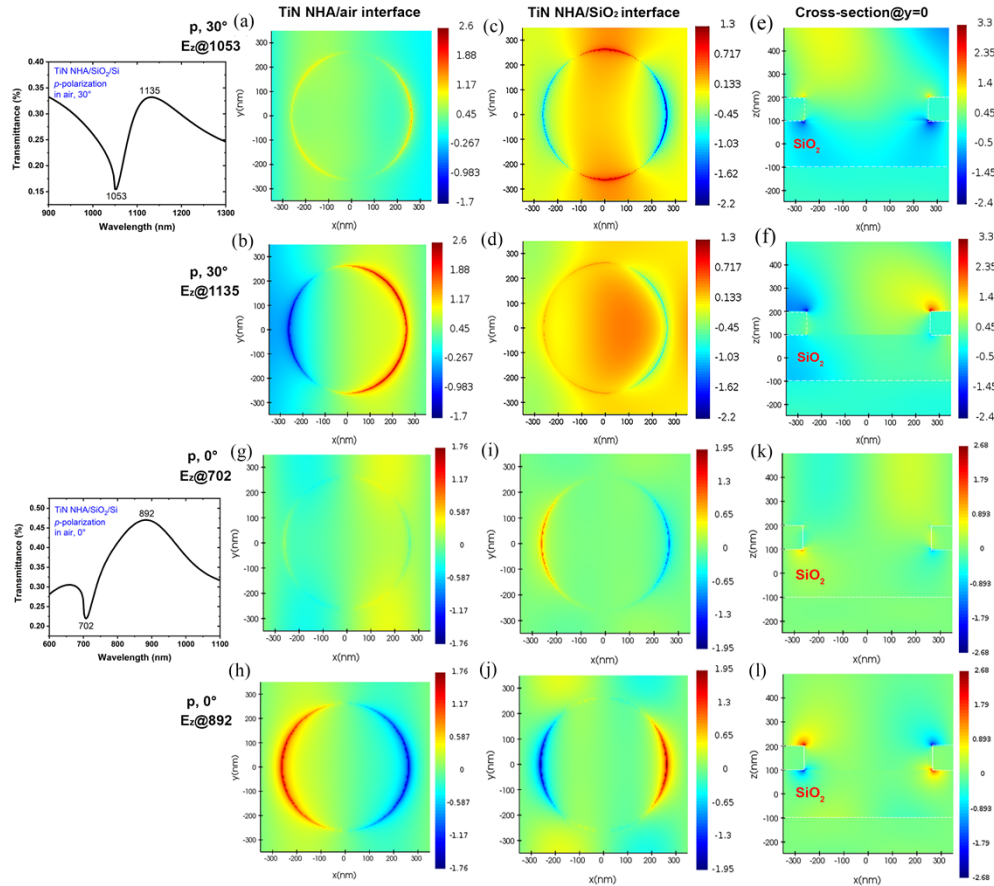


**Fig. 7.** *E<sub>z</sub>* distributions on top surface of TiN NHA, at the interface of TiN NHA and SiO<sub>2</sub>, and at the cross-section of the TiN NHA/SiO<sub>2</sub>/Si stack P700D540 at wavelength 1053 nm (a, c, e) and at 1135 nm (b, d, f) under illumination with *p*-polarized excitation at an angle of 30° to the propagating *z*-direction in air, and at wavelength 702 nm (g, i, k) and at 892 nm (h, j, l) under vertical *p*-polarized excitation. Transmittance of P700D540 under *p*-polarized excitation with an angle of 30° (left up image) and of 0° (left down image).

Comparing with the symmetric *E<sub>z</sub>* distribution under vertical incidence in Figs. 7(g) and 7(h), the *E<sub>z</sub>* distributions at the surface of the TiN NHA under oblique incidence exhibit an obvious asymmetry (Figs. 7(a) and 7(b)). The standing wave field pattern in *x*-direction is most obvious at vertical incidence (Figs. 7(g) and 7(h)). When looking at the cross-sectional plot of the *E<sub>z</sub>* at vertical incidence, a spatially extended RA feature at the top TiN NHA/superstrate interface can be identified at the wavelength corresponding to the dip in the transmittance (Fig. 7(k)).

At a slightly higher wavelength corresponding to the peak in transmittance, the shorter decay length visible in the  $E_z$  at the top TiN NHA/superstrate interface points towards the presence of SPP excitations (Fig. 7(l)). Field enhancements at the rim of the nanoholes are indicative of the presence of LSPRs in Figs. 7(i), 7(h), and 7(j). Furthermore, the sign of the  $E_z$  field on the top and bottom part of the nanohole's sidewall at vertical incidence with a wavelength of 892 nm (Fig. 7(l)) shows an anti-symmetric pattern that has been previously explained by interactions of SPP excitations with LSPR excitations [48].

When comparing with the case of vertical incidence, the  $E_z$  distributions under oblique incidence also resembles a standing wave pattern at the TiN NHA/air interface at 1053 nm (Fig. 7(a)). This pattern appears strongly distorted by the nanohole otherwise (Figs. 7(b) – 7(d)), especially at an excitation wavelength of 1135 nm corresponding to the transmittance peak and at the TiN NHA/SiO<sub>2</sub> interface (Fig. 7(d)). Furthermore, the maximum  $E_z$  amplitude directly at the rim of the nanohole is increased under oblique incidence. We attribute this to the fact that, while indications of the presence of LSPRs can be seen both for vertical and for oblique incidence, their coupling in particular to SPPs is enhanced at oblique incidence.

We briefly note here that while our investigation focuses on the effect of bulk refractive index changes on optical properties of our samples, for applications in biosensing and the detection of near-surface refractive index changes, i.e. in a thin surface layer on top of the NHA, is usually more relevant. In this case, the ratio of the thickness  $d$  of the surface layer to the decay length  $l_{decay}$ , i.e. the distance in  $z$ -direction over which the intensity of the evanescent field above the NHA/superstrate interface drops to  $1/e$  of the initial intensity, plays a role: the larger the ratio  $l_{decay}/d$ , the smaller the sensitivity with respect to the near-surface refractive index changes. This decay length increases with increasing angle of incidence [49], this can also be seen from comparing the  $E_z$  distributions shown in Fig. 7 (f) and Fig. 7 (l). As a result, there could be an optimum angle of incidence for the measurement of refractive index changes in a surface layer of a given thickness.

#### 4.2. Influence of Fabry-Pérot cavity modes on sensor performance

So far, we have argued that non-vertical light incidence leads both to a narrowing of the resonances by decreasing radiative losses and an increase in sensitivity as a result of increased interactions between LSPRs and SPPs. Interestingly, enhanced amplitudes of the  $E_z$  can be found in the SiO<sub>2</sub> layer under oblique incidence at 1053 nm (Fig. 7(e)) and 1135 nm (Fig. 7(f)), indicative of the fact that light is partially trapped within the SiO<sub>2</sub> layer. Therefore, we now investigate based on simulations how the sensing performance of the TiN NHAs can also be influenced by modifying the parameters of the layered substrate. As previous investigations have shown, the interplay of interface reflections with plasmonic excitations can have a significant influence on the peak shape for NHAs on layered substrates [19]. Indeed, as the diagrams in Fig. 6 show, the additional SiO<sub>2</sub>/Si interface in the TiN NHA/SiO<sub>2</sub>/Si layer stack compared to the TiN NHA/SiO<sub>2</sub> layer stack leads to a suppression of the peaks related to the SPP<sub>TiN-SiO<sub>2</sub></sub>(+1, 0) modes. As evidenced by the simulated distributions of the electromagnetic fields (Figs. 7(e) and 7(f)), the introduction of a thin SiO<sub>2</sub> layer between the TiN NHA and the Si substrate can also lead to the appearance of Fabry-Pérot cavity modes. The interplay of such cavity modes with plasmonic resonances has been shown previously to tune optical properties: Hybrid photonic-plasmonic cavity modes have been investigated for plasmonic particles placed on top of Fabry-Pérot cavities or waveguides formed by layered substrates, in single particle [50], dimer [51] or array [52] configuration. Furthermore, the combination of Fabry-Pérot cavities with Al NHAs has been analyzed under vertical incidence and at IR wavelengths [53]. Here, we focus on how a careful adjustment of the layer structure below the TiN NHA can be used to further boost sensor performance.

Since properties of Fabry-Pérot resonant modes will be strongly influenced by the thickness of the SiO<sub>2</sub> spacer layer (Figs. 7(e) and 7(f)), we performed FDTD simulations to systematically

evaluate the sensitivity (with a superstrate RI change from water ( $n = 1.33$ ) to ethanol ( $n = 1.36$ )) as a function of  $\text{SiO}_2$  thickness while keeping the thickness of TiN NHA constant. As shown in Fig. 8(a), the sensitivity peaks at a certain  $\text{SiO}_2$  thickness under excitation with  $p$ -polarized light at a fixed angle of incidence. The  $\text{SiO}_2$  thickness corresponding to the peak position increases with increasing incident angle as indicated by the dotted line, indicating that this trend originates from coupling to Fabry-Pérot cavity modes. The prerequisite for a resonance of an arbitrary cavity is that the accumulated phase shift of the wave during one complete round-trip as shown schematically for vertical incidence in Fig. 8(b) must be an integer multiple to  $2\pi$ . The total phase shift is the sum of phase shifts of propagation ( $\Delta\phi_{Prop}$ ) through the cavity ( $\text{SiO}_2$  layer) ( $\Delta\phi_{Prop} = 2t \cos \theta \cdot 2\pi / (\frac{\lambda}{n_{\text{SiO}_2}})$ ), where  $t$  is the thickness of  $\text{SiO}_2$  layer,  $\theta$  is the incident angle,  $n_{\text{SiO}_2}$  is the refractive index of  $\text{SiO}_2$ , the phase shifts upon reflection ( $\Delta\phi_{Refl}$ ) at the  $\text{SiO}_2/\text{Si}$  interface ( $\Delta\phi_{Refl} \approx \pi$ ), and the phase shifts upon reflection at the TiN NHA/ $\text{SiO}_2$  interface ( $\Delta\phi_{NHA}$ ), which is a priori unknown. These accumulated phase shifts satisfy the following equation:

$$2t \cos \theta \cdot \frac{2\pi}{\lambda_{\text{peak}}} \cdot n_{\text{SiO}_2} + \pi + \Delta\phi_{NHA} = 2\pi m. \quad m \in \mathbb{Z} \quad (3)$$

This allows us to compare  $\Delta\phi_{NHA}$  corresponding to the peak sensitivities as a function of incident angle and  $\text{SiO}_2$  thickness (Table 1), with the corresponding peak wavelengths  $\lambda_{\text{peak}}$  taken from simulated transmittance spectra (Fig. S14). The calculated  $\Delta\phi_{NHA}$  shows only a weak increase with increasing incident angle, giving further confirmation of the involvement of Fabry-Pérot resonant modes in the optical properties of our TiN NHA/ $\text{SiO}_2/\text{Si}$  sample.

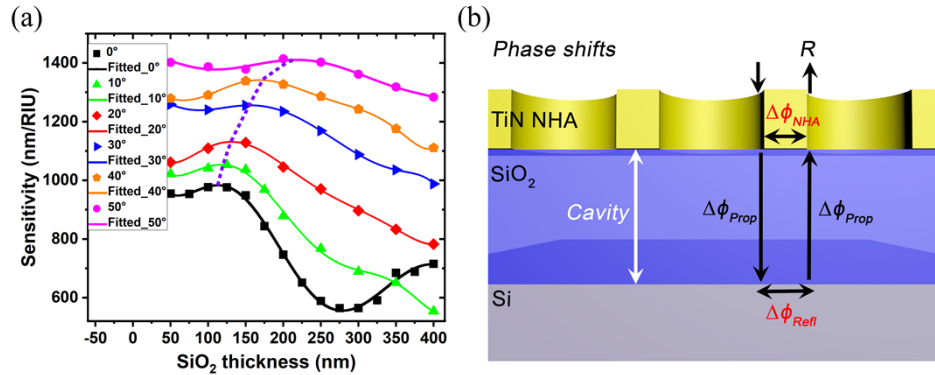


**Fig. 8.** Sensitivity of TiN NHA/ $\text{SiO}_2/\text{Si}$  stack P700D540 with respect to RI change from 1.33 to 1.36 under excitation angle from  $0^\circ - 50^\circ$  by FDTD when varying  $\text{SiO}_2$  thickness from 50 nm – 400 nm (a). Schematic of phase shifts of electromagnetic wave propagating in TiN NHA/ $\text{SiO}_2/\text{Si}$  during one roundtrip (b).

**Table 1.** Determined thickness of  $\text{SiO}_2$  layer ( $t$ ) and the resonant peak ( $\lambda_{\text{peak}}$ ) under oblique incidence, and the calculated phase shift of NHA ( $\Delta\phi_{NHA}$ ).

$\theta$ (deg)	$\theta$ (rad)	$t$ (nm)	$\lambda_{\text{peak}}$ (nm)	$\Delta\phi_{NHA}$ (rad)	$\Delta\phi_{NHA}/\pi$	$m$
0	0	110	1094	1.309475548	0.416819013	1
10	0.1745329	118	1217	1.401706811	0.446177135	1
20	0.3490659	130	1362	1.507299628	0.479788373	1
30	0.5235987	156	1501	1.501560344	0.477961502	1
40	0.6981317	173	1624	1.654657904	0.526693969	1
50	0.8726646	215	1732	1.687687971	0.537207766	1

In addition to the bulk sensitivity, the quantity FOM\* can also be employed to evaluate the performance of plasmonic sensors [54], and is defined as the amplitude shift  $\Delta A$  of the measured amplitude of the optical signal (such as reflectance or transmittance) upon a change of refractive index ( $\Delta n$ ) of the surrounding medium normalized by the signal amplitude ( $A$ ) at wavelength  $\lambda_{meas}$ , according to the following equation:

$$\text{FOM}^*(\lambda) = \left( \frac{\Delta A}{\Delta n} \right)_{\lambda_{meas}} \cdot A \quad (4)$$

This quantity is particularly important for refractive index sensing at a fixed wavelength of the incident light. Here, we used RCWA to evaluate FOM\* based on the reflectance spectra of a TiN NHA/SiO<sub>2</sub>/Si stack P700D540 with a fixed TiN layer thickness of 100 nm and a SiO<sub>2</sub> spacer layer with varied thickness 25–400 nm under *p*-polarized excitation with varied incident angle and for superstrate refractive indices  $n = 1.33$  and  $n = 1.36$  (Fig. 9). The wavelength at which FOM\* is evaluated changes as a function of angle of incidence. Here, the maximum FOM\* extracted for each spectrum is shown. Again, FOM\* is influenced not only by the incident angle but also by the thickness of the SiO<sub>2</sub> spacer layer and a peak value of 25.2 RIU<sup>-1</sup> is predicted for an angle of 70°, comparable to the performance of optimized Au nanorods for biosensing [54].

## 5. Conclusions

Realizing RI sensors based on plasmonic nanostructures as fully integrated, CMOS compatible devices requires, in particular, the use of CMOS compatible metals. The material TiN is an interesting candidate, however, large optical losses can limit its performance in plasmonic applications. Here, we investigated a TiN NHA on top of a layered substrate (TiN NHA/SiO<sub>2</sub>/Si) that was fabricated using a CMOS compatible process. The TiN NHA/SiO<sub>2</sub>/Si layer stacks exhibit Fano-type resonances in the reflectance spectra under *p*-polarized excitation with various angles of incidence in air. The angle of incidence strongly affects the optical properties of the TiN NHAs: Both experimental and simulated reflectance spectra show that the resonance linewidth is reduced at higher excitation angles – this is particularly important for materials such as TiN, in which strong ohmic losses negatively affect linewidths. Most importantly, the sensitivities determined from the reflectance spectra in air, in acetone and in water strongly increase with increasing incident angle of the light source. An extremely high sensitivity of 2305 nm RIU<sup>-1</sup> is predicted by simulation for a TiN NHA/SiO<sub>2</sub>/Si layer stack under *p*-polarized oblique excitation.

Our simulation results indicate that the interplay of plasmonic and photonic resonances, notably SPPs, LSPRs, RAs and Fabry-Pérot resonant modes, is at the origin of this behavior. We attribute the high sensitivities to a coupling between the LSPRs excited in the holes and the SPPs excited at the surface of the NHAs. The coupling to Fabry-Pérot resonant modes that form in the multilayer substrate can be used to further boost performance for refractive index sensing. This is particularly relevant since integrating plasmonic structures into optoelectronic devices usually requires those structures to be placed on top of a multilayer device stack – our simulation results show that this can be actively used to improve device performance and obtain a FOM\* as high as 25.2 RIU<sup>-1</sup>.

Our results confirm the potential for TiN as material for plasmonic applications, particularly when the use of CMOS compatible materials is required. By a careful variation specifically of the incident angle and the thickness of the SiO<sub>2</sub> spacer layer in our TiN NHA/SiO<sub>2</sub>/Si stacks, it is possible to strongly enhance their performance for refractive index sensing. Particularly high sensitivities can be attained when the material acting as a spacer layer between the TiN NHA and the Si substrate has a similar refractive index to that of the detected medium. The strong dependence of optical properties on the angle of incidence can also open up the possibility for utilizing the structures for angle-scanning refractometric sensors [55]. However, this also

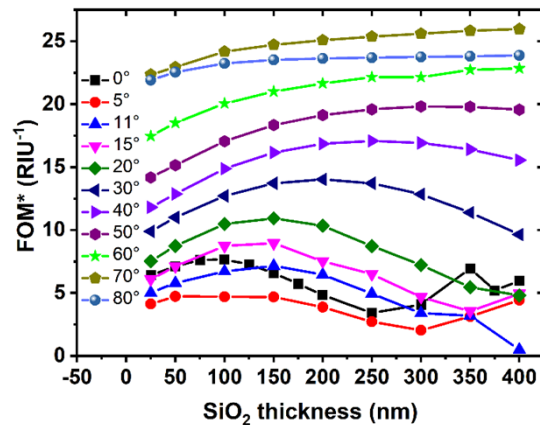


**Fig. 9.** Figure of merit star (FOM\*) of TiN NHA/SiO<sub>2</sub>/Si stack P700D540 with varied SiO<sub>2</sub> thickness obtained from reflectance spectra by RCWA when illuminated by *p*-polarized light source with incident angle of 0°, 5°, 11°, 15°, 20°, 30°, 40°, 50°, 60°, 70°, and 80° in superstrate of water and of ethanol.

means that the angle of incidence has to be carefully controlled in measurements, placing strict requirements on the light source.

Further performance improvements can also be expected from optimizing the deposition of the TiN layers: It was found previously that adjusting sputtering parameters can strongly improve the optical properties of the material [34,56,57]. It would also be interesting to investigate extended analytical models that can reproduce the position of Fano dips and peaks more faithfully, to facilitate further optimization. Nonetheless, our approach already shows great promise as a strategy to devise plasmonic sensors based on stacks containment of TiN as metallization for application in integrated, CMOS-compatible on-chip sensors.

**Funding.** Bundesministerium für Bildung und Forschung (16ES1128K, 16ME0420K).

**Acknowledgments.** The work was supported by the North-German Supercomputing Alliance (HLRN).

**Disclosures.** The authors declare no conflicts of interest.

**Data Availability.** Data underlying the results presented in this paper are available from the authors upon reasonable request.

**Supplemental document.** See Supplement 1 for supporting content.

## References

1. V. G. Kravets, A. V. Kabashin, W. L. Barnes, and A. N. Grigorenko, "Plasmonic Surface Lattice Resonances: A Review of Properties and Applications," *Chem. Rev.* **118**(12), 5912–5951 (2018).
2. S. Balbinot, A. M. Srivastav, J. Vidic, I. Abdulhalim, and M. Manzano, "Plasmonic biosensors for food control," *Trends Food Sci. Technol.* **111**, 128–140 (2021).
3. S. A. Maier, *Plasmonics: fundamentals and applications*. Springer: 2007; vol. 1.
4. J. Homola, S. S. Yee, and G. Gauglitz, "Surface plasmon resonance sensors: review," *Sens. Actuators, B* **54**(1-2), 3–15 (1999).
5. N. L. Kazanskiy, S. N. Khonina, and M. A. Butt, "Plasmonic sensors based on Metal-insulator-metal waveguides for refractive index sensing applications: A brief review," *Phys. E* **117**, 113798 (2020).
6. T. W. Ebbesen, H. J. Lezec, H. F. Ghaemi, T. Thio, and P. A. Wolff, "Extraordinary optical transmission through sub-wavelength hole arrays," *Nature* **391**(6668), 667–669 (1998).
7. J. Chen, F. Gan, Y. Wang, and G. Li, "Plasmonic Sensing and Modulation Based on Fano Resonances," *Adv. Opt. Mater.* **6**, 1701152 (2018).
8. A. B. Khanikaev, C. Wu, and G. Shvets, "Fano-resonant metamaterials and their applications," *Nanophotonics* **2**(4), 247–264 (2013).
9. M. Sarrazin, J.-P. Vigneron, and J.-M. Vigoureux, "Role of Wood anomalies in optical properties of thin metallic films with a bidimensional array of subwavelength holes," *Phys. Rev. B* **67**(8), 085415 (2003).

10. H. Gao, J. M. McMahon, M. H. Lee, J. Henzie, S. K. Gray, G. C. Schatz, and T. W. Odom, "Rayleigh anomaly-surface plasmon polariton resonances in palladium and gold subwavelength hole arrays," *Opt. Express* **17**(4), 2334 (2009).
11. C. Genet, M. P. van Exter, and J. P. Woerdman, "Fano-type interpretation of red shifts and red tails in hole array transmission spectra," *Opt. Commun.* **225**(4-6), 331–336 (2003).
12. B. Luk'yanchuk, N. I. Zheludev, S. A. Maier, N. J. Halas, P. Nordlander, H. Giessen, and C. T. Chong, "The Fano resonance in plasmonic nanostructures and metamaterials," *Nat. Mater.* **9**(9), 707–715 (2010).
13. A. Tao, P. Sinsersuksakul, and P. Yang, "Tunable plasmonic lattices of silver nanocrystals," *Nat. Nanotechnol.* **2**(7), 435–440 (2007).
14. A. E. Cetin, A. F. Coskun, B. C. Galarreta, M. Huang, D. Herman, A. Ozcan, and H. Altug, "Handheld high-throughput plasmonic biosensor using computational on-chip imaging," *Light: Sci. Appl.* **3**(1), e122 (2014).
15. B. Gjonaj, J. Aulbach, P. M. Johnson, A. P. Mosk, L. Kuipers, and A. Lagendijk, "Active spatial control of plasmonic fields," *Nat. Photonics* **5**(6), 360–363 (2011).
16. C. Escobedo, "On-chip nanohole array based sensing: a review," *Lab Chip* **13**(13), 2445 (2013).
17. P. R. West, S. Ishii, G. V. Naik, N. K. Emani, V. M. Shalae, and A. Boltasseva, "Searching for better plasmonic materials," *Laser Photonics Rev.* **4**(6), 795–808 (2010).
18. L. Augel, F. Berkmann, D. Latta, I. A. Fischer, S. Bechler, Y. Elogail, K. Kosteci, K. Potje-Kamloth, and J. Schulze, "Optofluidic sensor system with Ge PIN photodetector for CMOS-compatible sensing," *Microfluid. Nanofluid.* **21**(11), 169 (2017).
19. L. Augel, Y. Kawaguchi, S. Bechler, R. Körner, J. Schulze, H. Uchida, and I. A. Fischer, "Integrated Collinear Refractive Index Sensor with Ge PIN Photodiodes," *ACS Photonics* **5**(11), 4586–4593 (2018).
20. I. A. Fischer, M. Brehm, M. De Seta, G. Isella, D. J. Paul, M. Virgilio, and G. Capellini, "On-chip infrared photonics with Si-Ge-heterostructures: What is next?" *APL Photonics* **7**(5), 050901 (2022).
21. J. H. Park, S. E. Han, P. Nagpal, and D. J. Norris, "Observation of Thermal Beaming from Tungsten and Molybdenum Bull's Eyes," *ACS Photonics* **3**(3), 494–500 (2016).
22. P. Patsalas, N. Kalfagiannis, S. Kassavetis, G. Abadias, D. V. Bellas, C. Lekka, and E. Lidorikis, "Conductive nitrides: Growth principles, optical and electronic properties, and their perspectives in photonics and plasmonics," *Mater. Sci. Eng., R* **123**, 1–55 (2018).
23. M. Chirumamilla, A. Chirumamilla, Y. Yang, A. S. Roberts, P. K. Kristensen, K. Chaudhuri, A. Boltasseva, D. S. Sutherland, S. I. Bozhevolnyi, and K. Pedersen, "Large-Area Ultrabroadband Absorber for Solar Thermophotovoltaics Based on 3D Titanium Nitride Nanopillars," *Adv. Opt. Mater.* **5**, 1700552 (2017).
24. S. Ishii, R. P. Sugavaneshwar, and T. Nagao, "Titanium Nitride Nanoparticles as Plasmonic Solar Heat Transducers," *J. Phys. Chem. C* **120**(4), 2343–2348 (2016).
25. G. V. Naik, B. Saha, J. Liu, S. M. Saber, E. A. Stach, J. M. K. Irudayaraj, T. D. Sands, V. M. Shalae, and A. Boltasseva, "Epitaxial superlattices with titanium nitride as a plasmonic component for optical hyperbolic metamaterials," *Proc. Natl. Acad. Sci. U. S. A.* **111**(21), 7546–7551 (2014).
26. K. V. Sreekanth, Q. Ouyang, S. Sreejith, S. Zeng, W. Lishu, E. Ilker, W. Dong, M. ElKabbash, Y. Ting, C. T. Lim, M. Hinczewski, G. Strangi, K.-T. Yong, R. E. Simpson, and R. Singh, "Phase-Change-Material-Based Low-Loss Visible-Frequency Hyperbolic Metamaterials for Ultrasensitive Label-Free Biosensing," *Adv. Opt. Mater.* **7**, 1900081 (2019).
27. Ch. Mai, St. Marschmeyer, A. Peczek, A. Kroh, J. Jose, S. Reiter, I. A. Fischer, Ch. Wenger, and A. Mai, "Integration Aspects of Plasmonic TiN-based Nano-Hole-Arrays on Ge Photodetectors in a 200 mm Wafer CMOS Compatible Silicon Technology," *ECS Trans.*, (2022 (accepted)).
28. G. A. López-Muñoz, M. C. Estevez, E. C. Peláez-Gutierrez, A. Homs-Corbera, M. C. García-Hernandez, J. I. Imbaud, and L. M. Lechuga, "A label-free nanostructured plasmonic biosensor based on Blu-ray discs with integrated microfluidics for sensitive biodetection," *Biosens. Bioelectron.* **96**, 260–267 (2017).
29. Y. Kane, "Numerical solution of initial boundary value problems involving maxwell's equations in isotropic media," *IEEE Trans. Antennas Propag.* **14**(3), 302–307 (1966).
30. J. Schlipf and I. A. Fischer, "Rigorous coupled-wave analysis of a multi-layered plasmonic integrated refractive index sensor," *Opt. Express* **29**(22), 36201 (2021).
31. I. H. Malitson, "Interspecimen Comparison of the Refractive Index of Fused Silica," *J. Opt. Soc. Am.* **55**(10), 1205 (1965).
32. D. T. Pierce and W. E. Spicer, "Electronic Structure of Amorphous Si from Photoemission and Optical Studies," *Phys. Rev. B* **5**(8), 3017–3029 (1972).
33. G. V. Naik, J. Kim, and A. Boltasseva, "Oxides and nitrides as alternative plasmonic materials in the optical range [Invited]," *Opt. Mater. Express* **1**(6), 1090 (2011).
34. P. Patsalas, N. Kalfagiannis, and S. Kassavetis, "Optical Properties and Plasmonic Performance of Titanium Nitride," *Materials* **8**(6), 3128–3154 (2015).
35. <https://imagej.nih.gov/ij/index.html>.
36. J. Campo, F. Desmet, W. Wenseleers, and E. Goovaerts, "Highly sensitive setup for tunable wavelength hyper-Rayleigh scattering with parallel detection and calibration data for various solvents," *Opt. Express* **17**(6), 4587 (2009).
37. K.-L. Lee, C.-C. Chang, M.-L. You, M.-Y. Pan, and P.-K. Wei, "Enhancing the Surface Sensitivity of Metallic Nanostructures Using Oblique-Angle-Induced Fano Resonances," *Sci. Rep.* **6**(1), 33126 (2016).

38. W. Zhou and T. W. Odom, "Tunable subradiant lattice plasmons by out-of-plane dipolar interactions," *Nat. Nanotechnol.* **6**(7), 423–427 (2011).
39. M. Gao, W. Yang, Z. Wang, S. Lin, J. Zhu, and Z. Yang, "Plasmonic resonance-linewidth shrinkage to boost biosensing," *Photonics Res.* **8**(7), 1226 (2020).
40. L. S. Live, A. Dhawan, K. F. Gibson, H.-P. Poirier-Richard, D. Graham, M. Canva, T. Vo-Dinh, and J.-F. Masson, "Angle-dependent resonance of localized and propagating surface plasmons in microhole arrays for enhanced biosensing," *Anal. Bioanal. Chem.* **404**(10), 2859–2868 (2012).
41. J. C. Sharpe, J. S. Mitchell, L. Lin, N. Sedoglavich, and R. J. Blaikie, "Gold Nanohole Array Substrates as Immunobiosensors," *Anal. Chem.* **80**(6), 2244–2249 (2008).
42. A. Krishnan, T. Thio, T. J. Kim, H. J. Lezec, T. W. Ebbesen, P. A. Wolff, J. Pendry, L. Martin-Moreno, and F. J. Garcia-Vidal, "Evanescence coupled resonance in surface plasmon enhanced transmission," *Opt. Commun.* **200**(1-6), 1–7 (2001).
43. E. Shkondin, T. Repán, O. Takayama, and A. V. Lavrinenko, "High aspect ratio titanium nitride trench structures as plasmonic biosensor," *Opt. Mater. Express* **7**(11), 4171 (2017).
44. I. Tathfif, K. S. Rashid, A. A. Yaseer, and R. H. Sagor, "Alternative material titanium nitride based refractive index sensor embedded with defects: An emerging solution in sensing arena," *Results Phys.* **29**, 104795 (2021).
45. A. Lesuffleur, H. Im, N. C. Lindquist, and S.-H. Oh, "Periodic nanohole arrays with shape-enhanced plasmon resonance as real-time biosensors," *Appl. Phys. Lett.* **90**(24), 243110 (2007).
46. X. Liu, W. Liu, L. Fang, S. Ye, H. Shen, and B. Yang, "Highly sensitive deep-silver-nanowell arrays (d-AgNWAs) for refractometric sensing," *Nano Res.* **10**(3), 908–921 (2017).
47. Z. Chen, P. Li, S. Zhang, Y. Chen, P. Liu, and H. Duan, "Enhanced extraordinary optical transmission and refractive-index sensing sensitivity in tapered plasmonic nanohole arrays," *Nanotechnology* **30**(33), 335201 (2019).
48. S.-H. Chang, S. K. Gray, and G. C. Schatz, "Surface plasmon generation and light transmission by isolated nanoholes and arrays of nanoholes in thin metal films," *Opt. Express* **13**(8), 3150 (2005).
49. H. Gao, J.-C. Yang, J. Y. Lin, A. D. Stuparu, M. H. Lee, M. Mrksich, and T. W. Odom, "Using the Angle-Dependent Resonances of Molded Plasmonic Crystals To Improve the Sensitivities of Biosensors," *Nano Lett.* **10**(7), 2549–2554 (2010).
50. M. A. Schmidt, D. Y. Lei, L. Wondraczek, V. Nazabal, and S. A. Maier, "Hybrid nanoparticle–microcavity-based plasmonic nanosensors with improved detection resolution and extended remote-sensing ability," *Nat. Commun.* **3**(1), 1108 (2012).
51. S. Zhang, S. R. Panikkanvalappil, S. Kang, M. J. Smith, S. Yu, M. El-Sayed, and V. V. Tsukruk, "Enhancing Plasmonic–Photonic Hybrid Cavity Modes by Coupling of Individual Plasmonic Nanoparticles," *J. Phys. Chem. C* **123**(39), 24255–24262 (2019).
52. R. Ameling, L. Langguth, M. Hentschel, M. Mesch, P. V. Braun, and H. Giessen, "Cavity-enhanced localized plasmon resonance sensing," *Appl. Phys. Lett.* **97**(25), 253116 (2010).
53. B. Debbrecht, M. McElhiney, V. Carey, C. Cullen, M. S. Mirotznik, and B. G. DeLacy, "Cavity-based aluminum nanohole arrays with tunable infrared resonances," *Opt. Express* **25**(20), 24501 (2017).
54. J. Becker, A. Trügler, A. Jakab, U. Hohenester, and C. Sönnichsen, "The Optimal Aspect Ratio of Gold Nanorods for Plasmonic Bio-sensing," *Plasmonics* **5**(2), 161–167 (2010).
55. A. Leitis, A. Tittl, M. Liu, B. H. Lee, M. B. Gu, Y. S. Kivshar, and H. Altug, "Angle-multiplexed all-dielectric metasurfaces for broadband molecular fingerprint retrieval," *Sci. Adv.* **5**(5), eaaw2871 (2019).
56. M. N. Gadalla, A. S. Greenspon, M. Tamagnone, F. Capasso, and E. L. Hu, "Excitation of Strong Localized Surface Plasmon Resonances in Highly Metallic Titanium Nitride Nano-Antennas for Stable Performance at Elevated Temperatures," *ACS Appl. Nano Mater.* **2**(6), 3444–3452 (2019).
57. R. Mishra, C.-W. Chang, A. Dubey, Z.-Y. Chiao, T.-J. Yen, H. W. Howard Lee, Y.-J. Lu, and S. Gwo, "Optimized Titanium Nitride Epitaxial Film for Refractory Plasmonics and Solar Energy Harvesting," *J. Phys. Chem. C* **125**(24), 13658–13665 (2021).